Nanoscale

PAPER

View Article Online
View Journal | View Issue

Cite this: *Nanoscale*, 2020, **12**, 8364

Interfacial co-existence of oxygen and titanium vacancies in nanostructured TiO_2 for enhancement of carrier transport†

Yi Lu,[a,b] Yi-Xuan Liu,[a] Li He,[a] Li-Ying Wang,[c] Xiao-Long Liu,[b] Jia-Wen Liu,[a] Yuan-Zhou Li,[a] Ge Tian,*[a,d] Heng Zhao,[a] Xiao-Hang Yang,[e] Jie Liu,[a] Christoph Janiak,[f] Silvia Lenaerts,[g] Xiao-Yu Yang *[a,b,d] and Bao-Lian Su *[a,h]

Received 11th February 2020,
Accepted 21st February 2020

DOI: 10.1039/d0nr01180k

rsc.li/nanoscale

The interfacial co-existence of oxygen and metal vacancies in metal oxide semiconductors and their highly efficient carrier transport have rarely been reported. This work reports on the co-existence of oxygen and titanium vacancies at the interface between TiO_2 and rGO *via* a simple two-step calcination treatment. Experimental measurements show that the oxygen and titanium vacancies are formed under 550 °C/Ar and 350 °C/air calcination conditions, respectively. These oxygen and titanium vacancies significantly enhance the transport of interfacial carriers, and thus greatly improve the photocurrent performances, the apparent quantum yield, and photocatalysis such as photocatalytic H_2 production from water-splitting, photocatalytic CO_2 reduction and photo-electrochemical anticorrosion of metals. A new "interfacial co-existence of oxygen and titanium vacancies" phenomenon, and its characteristics and mechanism are proposed at the atomic-/nanoscale to clarify the generation of oxygen and titanium vacancies as well as the interfacial carrier transport.

Introduction

Titanium dioxide (TiO_2) is one of the most attractive semiconductors for photocatalysis, energy storage, and solar fuel technologies.[1–3] Defects are very important to tune the functional properties of semiconductors, as the surface and (or) interface vacancies are donor or acceptor type centers for the separation of photogenerated charges.[4,5] The interfacial co-existence of oxygen and titanium vacancies (O-vacancies and Ti-vacancies) is therefore a promising feature for highly efficient charge transfer at the atomic/nanoscale. Most recently, the fabrication of a homojunction of O-vacancies and Ti-vacancies in amorphous–anatase TiO_2 phases *via* a fast doping–filtration–drying approach in water solution has been demonstrated in our previous work.[6] Calcination at 350 °C is the key factor for the formation of Ti-vacancies. In practice, a high degree of crystallinity leads to a high condensation rate at the atomic level and might thus lead to more stablity.[7] However, there have rarely been reports on the co-existence of O-vacancies and Ti-vacancies in fully crystalline TiO_2, due to the calcination temperature of 350 °C which is very low for the transformation into the crystalline state.

Nanocarbons as foreign phase-junctions are very efficient dopants,[8,9] and are often used to capture oxygen atoms of TiO_2 thereby producing oxygen vacancies. As a research methodology, however, the formation of Ti-vacancies in the presence of carbon is theoretically and technologically irrational.[10] Graphene nanosheets as typical nanocarbon materials can capture the oxygen atoms of TiO_2 at high temperatures thereby creating O-vacancies. Graphene nanosheets act as a shell that confines small molecules/ions such as O species by unsatu-

[a]*State Key Laboratory of Advanced Technology for Materials Synthesis and Processing & School of materials science and engineering, Wuhan University of Technology, Wuhan, 430070, China. E-mail: xyyang@whut.edu.cn*
[b]*Southern Marine Science and Engineering Guangdong Laboratory (Zhuhai) & School of Chemical Engineering and Technology, School of Materials, Sun Yat-sen University, Zhuhai, 519000, China*
[c]*State Key Laboratory of Magnetic Resonance and Atomic and Molecular Physics, Wuhan Institute of Physics and Mathematics, The Chinese Academy of Sciences, Wuhan 430071, China*
[d]*School of Engineering and Applied Sciences, Harvard University, Cambridge, MA 02138, USA. E-mail: xyyang@seas.harvard.edu, gtian@seas.harvard.edu*
[e]*College of Chemistry, Jilin University, Changchun, 130023, China*
[f]*Institut für Anorganische Chemie und Strukturchemie, Heinrich-Heine-Universität Düsseldorf, 40204 Düsseldorf, Germany*
[g]*Research Group of Sustainable Energy and Air Purification (DuEL), Department of Bioscience Engineering, University of Antwerp, Antwerp, Belgium*
[h]*Laboratory of Inorganic Materials Chemistry (CMI), University of Namur, B-5000 Namur, Belgium. E-mail: bao-lian.su@unamur.be*

†Electronic supplementary information (ESI) available: Characterization, photocatalytic and photo-electrochemical experiments, SEM and TEM images, N_2 adsorption, XPS, PL emission, comparison of photocatalytic H_2 activity, and TG, UV-vis DRS, TRPL and OCP measurements. See DOI: 10.1039/d0nr01180k

rated defects and edge atoms.[11–13] The sp^2 bonded structure is the most thermodynamically stable state that is hard to oxidize, even at a calcination temperature of 350 °C. These unique features of graphene provide the opportunity to prepare TiO_2 that forms O-vacancies at high temperatures and simultaneously creates Ti-vacancies by confining the absorbed O species at relatively low temperatures. To the best of our knowledge, it is very rare to use reduced graphene oxide (rGO) for the formation of the Ti-vacancies. In this work, we present a two-step calcination treatment, starting with calcination at 500 °C in an Ar flow to form anatase TiO_2 with O-vacancy (denoted as TiO_2@rGO (first)) followed by calcination at 350 °C under air conditions to induce Ti-vacancies, assisted by rGO sheets (denoted as TiO_2@rGO). These interfacial O-vacancies and Ti-vacancies in fully crystalline TiO_2 significantly enhance the transport of interfacial carriers, and thus greatly improve the photochemical and photo-electrochemical performance of TiO_2.

Results and discussion

The scanning electron microscopy (SEM) image of the TiO_2 beads shows a uniform size of about 400 nm and their aggregation from smaller nanoparticles (Fig. 1a). High-resolution transmission electron microscopy (HRTEM) further confirms the sphere-like structure of TiO_2 constructed from nanocrystals with a size of about 15 nm (Fig. 1b), and a spacing of 0.35 nm is assigned to the (101) plane of anatase TiO_2. The X-ray diffraction (XRD) patterns of the TiO_2 precursor bead, TiO_2 and TiO_2@rGO are shown in the inset of Fig. 1c. No peak is observed for the amorphous TiO_2 precursor bead. The diffraction peaks of both TiO_2 and TiO_2@rGO upon calcination treatment display a crystalline anatase phase (ICDD no. 21-1272).[14] No obvious peak changes occur after rGO coating, indicating that the coating with rGO does not influence the crystal structure of TiO_2. The SEM and TEM images of TiO_2@rGO show that TiO_2 beads are successfully coated with thin rGO layers, which might be favourable charge transfer (Fig. 1c and d). As observed in Fig. 1e, the ultra-thin rGO sheets with a thickness of 3–5 nm are intimately coated on the external surface of TiO_2 beads. The lattice distortions between rGO sheets and TiO_2 can be clearly seen in the inverse fast Fourier transform (FFT) image (Fig. 1f). This nano-fusion domain has a thickness of around 1 nm and can interconnect with ordered lattice fringes of TiO_2 and rGO layers, allowing the quantized ballistic transport of electrons and therefore is beneficial for the enhancement of carrier mobility and minimization of energy loss.[6,15] Notably, the outermost rGO is not an entirely continuous phase and exposes more defect atoms, which could be attributed to the fragmentation of rGO sheets during the two-step calcination. Both TiO_2 and TiO_2@rGO nitrogen sorption isotherms show the final saturation plateau with H2(b) hysteresis loops, indicating type IV isotherms (Fig. S2†).[16] The increase in adsorption at high partial pressures (P/P_0 > 0.9) can be attributed to the inter-particle volume of the aggregated beads (Fig. 1a and b) forming a mesoporous cavity. The pore size of TiO_2 is maintained at 13 nm after compositing with rGO (Table S1†). From the Raman spectra shown in Fig. S3,† the peaks at 150 cm^{-1} (E_g), 394 cm^{-1} (B_{1g}), 510 cm^{-1} (A_{1g}), and 629 cm^{-1} (E_g) are attributed to the anatase crystallites of TiO_2.[17] Furthermore evaluation of the I_D/I_G intensity ratio (0.982 for GO and 1.099 for TiO_2@rGO) reveals a fragmentation of sp^2 domains,[18] due to the increase in the number of unsaturated defect atoms of rGO that provides more sites to confine the oxygen species.

For comparison, the as-prepared TiO_2 precursor was calcined at 500 °C in an Ar flow (denoted as TiO_2 (first)) and then at 350 °C in air (denoted as TiO_2), and the as-prepared TiO_2@rGO precursor was calcined at 500 °C in an Ar flow and denoted as TiO_2@rGO (first). As shown in Fig. 2, the strong electron paramagnetic resonance (EPR) signal at g = 2.002 in TiO_2@rGO is attributed to the O-vacancies in TiO_2 lattices, while the weak signal at g = 1.965 in TiO_2@rGO is attributed to the Ti^{3+} defects associated with O-vacancies.[19] The signal at g = 2.010 is attributed to the O^- species usually accompanied by Ti-vacancies.[20,21] In contrast, the EPR spectra of rGO exhibit a

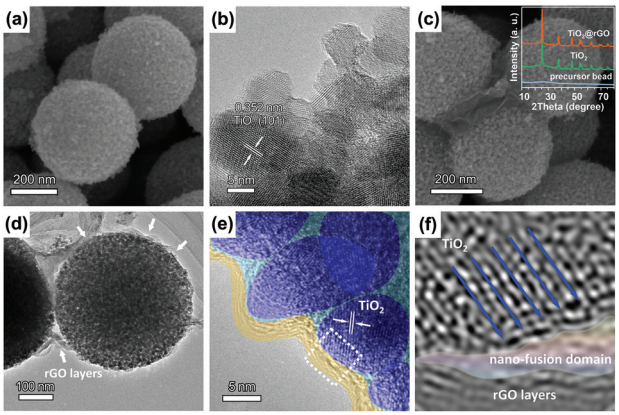

Fig. 1 (a) SEM and (b) TEM image of TiO_2, (c) SEM image of TiO_2@rGO, the inset shows the XRD patterns of precursor bead, TiO_2 and TiO_2@rGO. (d) TEM image of TiO_2@rGO. (e) HRTEM images of nanocrystalline domains of anatase TiO_2 (blue area), amorphous TiO_2 (pale blue area) and rGO (yellow area). (f) The inverse FFT pattern from the white dotted area.

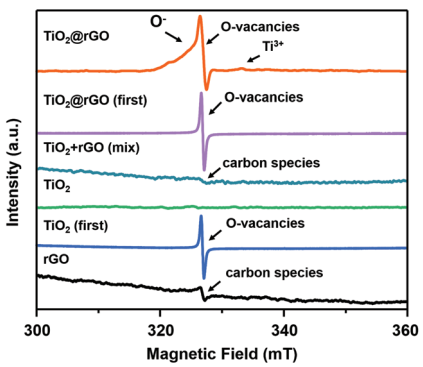

Fig. 2 EPR spectra of different samples at room temperature.

signal at g = 2.002 attributed to the unsaturated defects and edge atoms on the rGO sheets.[22] After the second calcination treatment, the signal at g = 2.002 in TiO_2 is absent while this signal in TiO_2@rGO is fully retained, indicating that the O-vacancies are stabilized in TiO_2@rGO in comparison with TiO_2. The signal at g = 2.002 with a very weak intensity observed in TiO_2 + rGO (mixture) is attributed to the low amount of rGO in the mixture. Only one signal at g = 2.002 is observed in TiO_2@rGO (first), suggesting that the second calcination (350 °C-air) produces Ti-vacancies in oxygen-deficient TiO_2. Notably, without coating of a rGO layer, TiO_2 (first) shows no signal at g = 2.010 and only a weak signal at g = 2.002 after the first calcination (500 °C-Ar), indicating that rGO is a critical and necessary factor for the interfacial co-existence of O-vacancies and Ti-vacancies. These results imply that Ti-vacancies are successfully induced *via* calcination at 350 °C in air, while the rGO plays an important role in producing defects of oxygen and titanium.

2D ^{1}H DQ magic angle spinning (MAS) NMR spectroscopy can investigate proton–proton interactions and is thus employed to investigate the types of Ti–OH group in TiO_2 materials. As shown in Fig. 3, the 2D ^{1}H DQ MAS NMR spectrum of TiO_2 (first) shows diagonal peaks at (0.30, 0.60) and (1.12, 2.24) ppm attributed to the autocorrelation between terminal hydroxyl groups on the surface, and the diagonal peaks of TiO_2 (first) and TiO_2@rGO (first) at (8.35, 16.70) and (7.9, 16.80) ppm both assigned to the hydrogen bond in bridging hydroxyl groups (Ti–O–H···O) in the bulk lattice.[23] After the two-step calcination, the intense off-diagonal peak pairs at (9.03, 9.03 + 2.74) and (2.74, 2.74 + 9.03) ppm are observed for TiO_2@rGO and correspond to the spatial correlation between the terminal hydroxyl groups and the bridging hydroxyl groups, which is beneficial to the adsorption of H_2O, and act as the active species for the photocatalytic reaction.[24,25] Interestingly, new autocorrelation peaks appear at (3.75, 7.50) and (3.90, 7.80) ppm for TiO_2 and TiO_2@rGO samples, respectively. Based on our previous work, they can be attributed to the spatial proximity of the hydrogen atom in Ti–OH nests to the Ti-vacancies.[6] Besides, the signal intensity of Ti–OH nests in TiO_2@rGO is stronger than that in pure TiO_2, combined with the EPR results, we can conclude that the core–shell structure with a two-step calcination treatment is critical for the production of Ti-vacancies by the confinement effect.

To further confirm the surface defect states, X-ray photoelectron spectroscopy (XPS) is utilized. From the C 1s spectra of TiO_2 and TiO_2@rGO in Fig. 4a, the deconvoluted peaks centered at 284.8 eV and 288.8 eV can be assigned to C–C/C=C and C=O bonds, respectively. In TiO_2@rGO a relatively strong peak centered at 284 eV is attributed to the Ti–C bond,[26–28] which indicates a strong interaction between TiO_2 and rGO. The peak of TiO_2 centered at 286.25 eV is attributed to the C–OH bond, while a blue shift in the binding energy of the C–O bond to 286.45 eV in TiO_2@rGO might be due to the formation of a C–O–Ti bond.[29] In the XPS Ti $2p_{3/2}$ spectrum of TiO_2@rGO in Fig. 4b, the main peak at a binding energy of 458.8 eV is attributed to Ti^{4+}. The peak at a binding energy of 459.6 eV is attributed to the Ti–C bond,[30,31] which is consistent with C 1s analysis. Another peak of Ti $2p_{3/2}$ at 458.4 eV is attributed to Ti^{3+}, which is usually accompanied by O-vacancies.[32,33] In addition, the three peak deconvolutions centered at 529.9 eV, 530.8 eV and 532 eV in the XPS O 1s spectrum of TiO_2@rGO correspond to O^{2-}, O^- and –OH, respectively (Fig. 4c). The deconvolution of the O^- peak correlating with the titanium vacancies is weak, because the Ti-vacancies are formed only at the interface between the O-vacancy rich TiO_2 and rGO. Technically, the Ti-vacancies are not easily detected by a single characterization method. More evidence for the presence of Ti-vacancies is shown in the EPR and 2D ^{1}H DQ MAS NMR spectra. In contrast, the signals of the Ti–C bond, Ti^{3+}, and O^- cannot be detected in TiO_2, indicating that the Ti-vacancies are formed at the surface/interface of

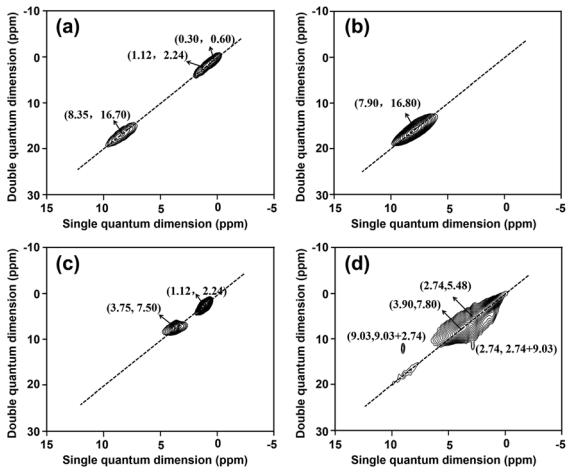

Fig. 3 2D ^{1}H DQ MAS NMR spectra of (a) TiO_2 (first), (b) TiO_2@rGO (first), (c) TiO_2 and (d) TiO_2@rGO.

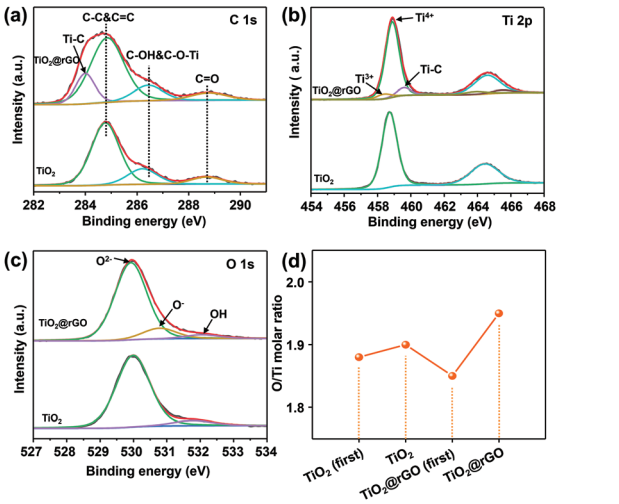

Fig. 4 (a) C 1s, (b) Ti 2p and (c) O 1s XPS spectra of TiO_2 and TiO_2@rGO. (d) The surface molar ratio of Ti : O from the XPS spectra of TiO_2 (first), TiO_2, TiO_2@rGO (first) and TiO_2@rGO.

TiO_2@rGO and trace amount of Ti-vacancies are formed in TiO_2. However, the enhancement of the O/Ti ratio does not represent the stoichiometry of TiO_2, Fig. 4d reflects the changing trend of surface/interface Ti-vacancies (Fig. S4 and Table S2†).

The arc radius in the EIS Nyquist plot denotes the resistance (R_{ct}) of the charge transfer at the electrode/electrolyte interfaces. As shown in Fig. 5a, TiO_2@rGO (first) and TiO_2@rGO have smaller R_{ct} than TiO_2 (first) and TiO_2 under dark conditions, implying that the coating of rGO on TiO_2 is beneficial for the surface charge transfer. Notably, TiO_2@rGO exhibits the most decreased R_{ct} compared to other samples after light irradiation, suggesting that TiO_2@rGO shows the most effective separation of photogenerated charges. This results in fast interfacial charge transfer to the electron donor or acceptor, that benefits from the interfacial co-existence of O-vacancies and Ti-vacancies. The photoluminescence (PL) intensity of TiO_2@rGO after excitation shows evident PL quenching (Fig. S5†), further confirming the more efficient extraction of photogenerated carriers after the introduction of rGO, O-vacancies and Ti-vacancies. The charge transfer is also confirmed by the transient photocurrent response (Fig. 5b); TiO_2@rGO exhibits the highest photocurrent intensity which is 2.0-fold, 4.3-fold and 9.2-fold higher compared to those of TiO_2@rGO (first), TiO_2 and TiO_2 (first), respectively. These results strongly confirm that TiO_2@rGO with the interfacial co-existence of O-vacancies and Ti-vacancies exhibit better carrier transport than TiO_2@rGO (first) with O-vacancies, TiO_2 and TiO_2 (first).

The photocatalytic H_2 production from water-splitting of samples is measured under the UV-vis light irradiation. As shown in Fig. 6, inadequate or excessive coating with rGO leads to a lowered H_2 yield efficiency, and the initial GO content of 1.5 wt% was optimal in TiO_2@rGO, the corresponding rGO content in final TiO_2@rGO is 0.5 wt% as determined by TGA analysis (Fig. S6†). As we all know, the absorbance of each component of heterojunction materials is a critical factor for the photocatalytic activity and thus may hinder the accurate evaluation of photocatalysts.[34,35] To better understand the comparison of photocatalytic activity, we synthesized the core–shell structured TiO_2–rGO without interfacial vacancies by direct coating as the reference samples. It should be noted that all samples showed nearly no photocatalytic

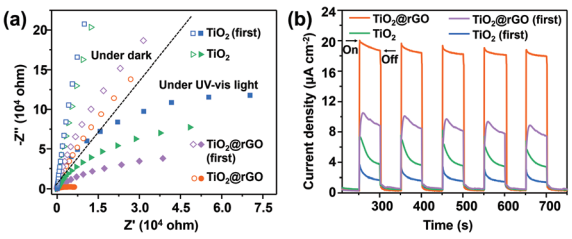

Fig. 5 (a) EIS Nyquist plots in the dark and under UV-vis light irradiation and (b) transient photocurrent response of TiO_2 (first), TiO_2, TiO_2@rGO (first) and TiO_2@rGO.

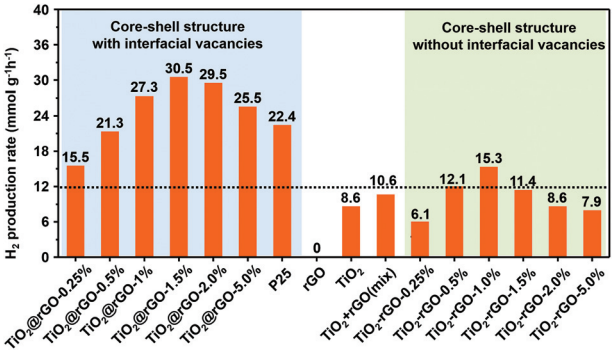

Fig. 6 Photocatalytic H_2 production rates of TiO_2, P25, rGO, TiO_2 + rGO (mixture), TiO_2@rGO (the weight ratios of GO to TiO_2 precursor were 0.25 wt%, 0.5 wt%, 1.0 wt%, 1.5 wt%, 2.0 wt% and 5 wt%) and corresponding core–shell structured TiO_2-rGO (the weight ratios of rGO to TiO_2 precursor were 0.25 wt%, 0.5 wt%, 1.0 wt%, 1.5 wt%, 2.0 wt% and 5.0 wt%). The experiment was carried out in water/methanol solution under UV-vis light irradiation, 0.5 wt% of Pt was loaded and acted as a co-catalyst.

activity in the visible light region and all the TiO_2 and the TiO_2 and rGO composites showed photocatalytic activity only in the ultraviolet region (Fig. 6 and Table S3†), although the TiO_2 and rGO composite showed enhanced visible light absorption intensity (Fig. S7†). Therefore, there is a simple relationship between UV light absorption and nanocomposites in our work. Experiments show that the photocatalytic H_2 production rate of the TiO_2@rGO-1.5% sample (rGO weight: 0.5 wt%) is 2.5-fold and 2.9-fold those of TiO_2–rGO-0.5% (rGO weight: 0.5 wt%, without any vacancy and a similar core–shell structure to TiO_2@rGO) and TiO_2 + rGO (mixture) (rGO weight: 0.5 wt%, without any vacancy and core–shell structure), respectively, as shown in Fig. 6. These results indicate that the introduction of interfacial vacancies in the TiO_2@rGO structure is of vital importance to enhance the photoactivity while rGO or the core–shell structure plays a part role. Moreover, compared with the non-vacancy structure (TiO_2–rGO), TiO_2@rGO exhibits satisfactory photocatalytic stability (96% of the initial photoactivity) after 5 cycles (25 h) under UV-vis light irradiation compared to only 60% for TiO_2–rGO (Fig. S8†). From the 2D ^{1}H DQ MAS NMR spectrum of TiO_2@rGO after 5 cycles of photocatalytic H_2 production reaction, the diagonal peak at (3.90, 7.80) ppm corresponding to the spatial proximity of Ti–OH nests to the Ti-vacancies show almost no change (Fig. S9†), suggesting a high photocatalytic stability of the interfacial vacancy structure at the atomic level.

Evaluation of the interfacial vacancies based on photocatalytic performances is shown in Fig. 7. TiO_2@rGO (1.5 wt% of GO) exhibits as much as 2.9 mmol of H_2 production after 5 h reaction (apparent quantum yield at 365 nm was calculated to be 12.9%), which is about 1.4-fold, 2.3-fold, 3.3-fold and 3.9-fold those of commercial TiO_2 (P25), TiO_2@rGO (first), TiO_2 and TiO_2 (first), respectively. It should be noted that the photocatalytic performance of TiO_2 without O-vacancies is just higher than that of TiO_2 (first) with O-vacancies. The only difference is of the presence of amorphous carbon in the

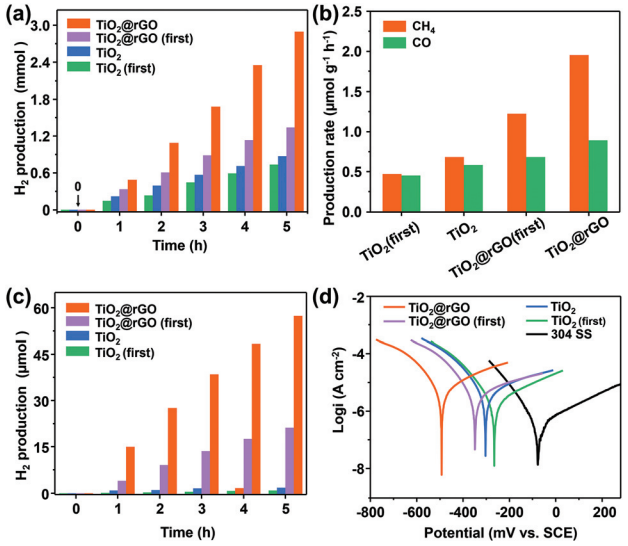

Fig. 7 Photocatalytic and photo-electrochemical performances. (a) Photocatalytic H_2 production in water/methanol over time, 0.5 wt% of Pt was loaded as a co-catalyst. (b) Evolution of CH_4 and CO over samples, without adding any sacrificial agent and co-catalyst. (c) Photocatalytic H_2 production in seawater over time, without adding any sacrificial agent and co-catalyst. (d) Tafel curves of bare 304 SS electrode and 304 SS coupled with the prepared photoelectrodes.

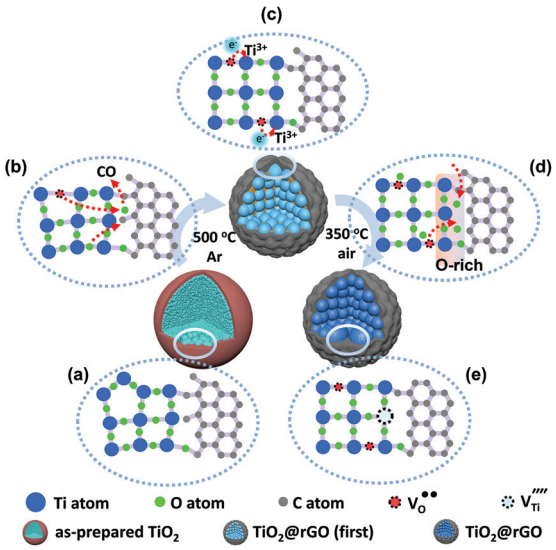

Fig. 8 Schematic illustration of the formation mechanism of O-vacancies and Ti-vacancies. (a) As prepared TiO_2@rGO, obtained by the hydrothermal process. (b) O atoms migrate from the lattice to interface and are captured by C atoms. (c) O-Vacancies in TiO_2@rGO after the first calcination treatment. (d) Adsorption and confinement of the O species. (e) Interfacial co-existence of O-vacancies and Ti-vacancies in TiO_2@rGO.

mesochannels of TiO_2 (first), due to the carbonization of the surfactant during the first calcination step. Probably, this amorphous carbon influences the mass diffusion, light absorption and electron utilization. According to the above analysis, we can conclude that the second calcination and interfacial Ti-vacancies are key factors for the order of magnitude enhancement of the photocatalytic performance. More evidence is obtained from time-resolved transient photoluminescence (TRPL) analysis, giving the fluorescence lifetimes of 1.55, 1.82, 1.88, 2.65, 2.97 and 3.64 ns for TiO_2 (first), TiO_2, TiO_2–rGO-0.5%, TiO_2@rGO (first), p25 and TiO_2@rGO (Fig. S10†), respectively, which further confirms the superiority of TiO_2@rGO for photogenerated charge separation and transfer. Utilization of solar energy and conversion of CO_2 to hydrocarbon fuels are highly desirable. The photocatalytic CO_2 reduction performance of the samples is examined in neutral water under UV-vis light irradiation without any sacrificial reagents or co-catalysts. TiO_2@rGO exhibits 4.1-fold CH_4 production rate and 1.3-fold (from 51.1% to 68.7%) CH_4 selectivity compared to TiO_2 (first) (Fig. 7b). Due to the excellent corrosion resistance of TiO_2 and graphene materials to seawater, our interfacial vacancy structures are studied under seawater conditions for potential marine applications. Similarly, the TiO_2@rGO demonstrates a 70.7-fold H_2 production rate increase from photocatalytic seawater splitting compared to TiO_2 (first) without adding any sacrificial agent and co-catalysts (Fig. 7c), in addition to a 6.6-fold increase in corrosion potential (−76 mV to −501 mV) compared with TiO_2 (first) towards photo-electrochemical anticorrosion of seawater (Fig. 7d, Fig. S11 and Table S4†). These remarkable performances in seawater are mainly attributed to the stable core–shell structure and readily accessible electrons at the interface, which reduced the interference from the various ionic components and impurities in seawater. These results indicate that structure of TiO_2@rGO facilitates the photogenerated charge separation and transfer in photocatalysis and photoelectrochemical anticorrosion.

As illustrated in Fig. 8, strong Ti–C and Ti–O–C chemical bonds are generated at the interface of TiO_2 and rGO after the hydrothermal treatment (Fig. 8a). The C atoms near the TiO_2 lattice capture a fraction of interfacial lattice O atoms upon calcination at 500 °C in an Ar flow (Fig. 8b, Fig. S6†), leaving O-vacancies with Ti^{3+} species to balance the charge (Fig. 8c).[36] The formation of O-vacancies can be described as:

$$O_O + \frac{1}{2}C \rightarrow V_O^{\cdot\cdot} + 2e' + \frac{1}{2}CO_2 \quad (1)$$

$$2e' + 2Ti_{Ti} \rightarrow 2Ti'_{Ti} \quad (2)$$

where O_O represents lattice O^{2-}, Ti_{Ti} represents lattice Ti^{4+}, $V_O^{\cdot\cdot}$ represents an O-vacancy, e′ represents an electron, O_M^x represents migrating oxygen atoms and Ti'_{Ti} represents lattice Ti^{3+}. Following the calcination treatment at 350 °C in air, the O species[6,11,20] (possibly including adsorption oxygen, surface oxygen and interstitial oxygen) migrate to the TiO_2 and rGO interface, and bind at the interface at the relatively low calcination temperature (Fig. 8d), resulting in O-rich domains that lead to distortions and concomitant Ti-vacancies (Fig. 8e). O^-

species near Ti-vacancies could be formed to balance the charge. The formation of Ti-vacancies can be described as

$$O_M^x \rightarrow \frac{1}{2}O_2 \quad (3)$$

$$O_2 \rightarrow 2O_O + V''''_{Ti} + 4h^{\bullet} \quad (4)$$

where V''''_{Ti} stands for a Ti-vacancy and $h^{\bullet}$ stands for a hole. Finally, a structure with co-existence of O-vacancies and Ti-vacancies forms at the interface of the TiO_2 and rGO. The interfacial carrier transport, starting from the inner lattice and O-vacancies to Ti-vacancies and to rGO sheets is facilitated.

Conclusions

In summary, a composite with interfacial co-existence of O-vacancies and Ti-vacancies of TiO_2 confined by rGO has been successfully fabricated through a two-step calcination strategy, and greatly improves the carrier transport. The impressive photochemical and photo-electrochemical performances are attributed to the unique electron pathway from O-vacancies to Ti-vacancies, and to the rGO layer. The TiO_2@rGO exhibits intriguing interfacial O-vacancies and Ti-vacancies tunable by the design of the O-rich interface confined by rGO at relatively low temperatures while opening the door to for investigating the nature of semiconductors and for their high-performance design.

Conflicts of interest

There are no conflicts to declare.

Acknowledgements

This work was supported by the National Natural Science Foundation of China (51861135313, U1663225, U1662134, and 51472190), the International Science & Technology Cooperation Program of China (2015DFE52870), the Program for Changjiang Scholars and Innovative Research Team in University (IRT_15R52), the Fundamental Research Funds for the Central Universities (19lgpy113 and 19lgzd16), the Jilin Province Science and Technology Development Plan (20180101208JC) and the Hubei Provincial Natural Science Foundation of China (2016CFA033).

Notes and references

1 J. Schneider, M. Matsuoka, M. Takeuchi, J. Zhang, Y. Horiuchi, M. Anpo and D. W. Bahnemann, *Chem. Rev.*, 2014, **114**, 9919–9986.
2 S. Xiao, Y. Lu, X. Li, B.-Y. Xiao, L. Wu, J.-P. Song, Y.-X. Xiao, S.-M. Wu, J. Hu, Y. Wang, G.-G. Chang, G. Tian, S. Lenaerts, C. Janiak, X.-Y. Yang and B.-L. Su, *Chem. – Eur. J.*, 2018, **24**, 13246–13252.
3 I. Roger, M. A. Shipman and M. D. Symes, *Nat. Rev. Chem.*, 2017, **1**, 0003.
4 J. Nowotny, T. Bak, M. K. Nowotny and L. R. Sheppard, *J. Phys. Chem. B*, 2006, **110**, 18492–18495.
5 P. Winget, L. K. Schirra, D. Cornil, H. Li, V. Coropceanu, P. F. Ndione, A. K. Sigdel, D. S. Ginley, J. J. Berry, J. Shim, H. Kim, B. Kippelen, J.-L. Brédas and O. L. A. Monti, *Adv. Mater.*, 2014, **26**, 4711–4716.
6 S.-M. Wu, X.-L. Liu, X.-L. Lian, G. Tian, C. Janiak, Y.-X. Zhang, Y. Lu, H.-Z. Yu, J. Hu, H. Wei, H. Zhao, G.-G. Chang, G. Tendeloo, L.-Y. Wang, X.-Y. Yang and B.-L. Su, *Adv. Mater.*, 2018, **30**, 1802173.
7 J. Tzadikov, M. Amsellem, H. Amlani, J. Barrio, A. Azoulay, M. Volokh, S. Kozuch and M. Shalom, *Angew. Chem., Int. Ed.*, 2019, **58**, 14964–14968.
8 J. J. Vilatela and D. Eder, *ChemSusChem*, 2012, **5**, 456–478.
9 K. C. Christoforidis and P. Fornasiero, *ChemCatChem*, 2017, **9**, 1523–1544.
10 J. Tang, Y. Liu, Y. Hu, G. Lv, C. Yang and G. Yang, *Chem. – Eur. J.*, 2018, **24**, 4390–4398.
11 K. Wong, S. J. Kang, C. W. Bielawski, R. S. Ruoff and S. K. Kwak, *J. Am. Chem. Soc.*, 2016, **138**, 10986–10994.
12 S. T. Bulbula, Y. Dong, Y. Lu and X.-Y. Yang, *Chem. Lett.*, 2018, **47**, 210–212.
13 K. G. Zhou, K. S. Vasu, C. T. Cherian, M. Neek-Amal, J. C. Zhang, H. Ghorbanfekr-Kalashami, K. Huang, O. P. Marshall, V. G. Kravets, J. Abraham, Y. Su, A. N. Grigorenko, A. Pratt, A. K. Geim, F. M. Peeters, K. S. Novoselov and R. R. Nair, *Nature*, 2018, **559**, 236–240.
14 Y. Dong, S.-Y. Chen, Y. Lu, Y.-X. Xiao, J. Hu, S.-M. Wu, Z. Deng, G. Tian, G.-G. Chang, J. Li, S. Lenaerts, C. Janiak, X.-Y. Yang and B.-L. Su, *Chem. – Asian J.*, 2018, **13**, 1609–1615.
15 Y. Lu, X. Cheng, G. Tian, H. Zhao, L. He, J. Hu, S.-M. Wu, Y. Dong, G.-G. Chang, S. Lenaerts, S. Siffert, G. Van Tendeloo, Z.-F. Li, L.-L. Xu, X.-Y. Yang and B.-L. Su, *Nano Energy*, 2018, **47**, 8–17.
16 M. Thommes, K. Kaneko, A. V. Neimark, J. P. Olivier, F. Rodriguez-Reinoso, J. Rouquerol and K. S. W. Sing, *Pure Appl. Chem.*, 2015, **87**, 1051–1069.
17 J. Zhang, M. Li, Z. Feng, J. Chen and C. Li, *J. Phys. Chem. B*, 2006, **110**, 927–935.
18 S. Stankovich, D. A. Dikin, R. D. Piner, K. A. Kohlhaas, A. Kleinhammes, Y. Jia, Y. Wu, S. B. T. Nguyen and R. S. Ruoff, *Carbon*, 2007, **45**, 1558–1565.
19 S. Wang, L. Pan, J.-J. Song, W. Mi, J.-J. Zou, L. Wang and X. Zhang, *J. Am. Chem. Soc.*, 2015, **137**, 2975–2983.
20 J. Strunk, W. C. Vining and A. T. Bell, *J. Phys. Chem. C*, 2010, **114**, 16937–16945.
21 W. Wang, C. Lu, Y. Ni, M. Su and Z. Xu, *Appl. Catal., B*, 2012, **127**, 28–35.
22 Y. Zhu, S. Murali, M. D. Stoller, K. J. Ganesh, W. Cai, P. J. Ferreira, A. Pirkle, R. M. Wallace, K. A. Cychosz, M. Thommes, D. Su, E. A. Stach and R. S. Ruoff, *Science*, 2011, **332**, 1537–1541.
23 F. Liu, N. Feng, Q. Wang, J. Xu, G. Qi, C. Wang and F. Deng, *J. Am. Chem. Soc.*, 2017, **139**, 10020–10028.

24 P. Salvador, *J. Phys. Chem. C*, 2007, **111**, 17038–17043.
25 A. Imanishi, T. Okamura, N. Ohashi, R. Nakamura and Y. Nakato, *J. Am. Chem. Soc.*, 2007, **129**, 11569–11578.
26 O. Akhavan and E. Ghaderi, *J. Phys. Chem. C*, 2009, **113**, 20214–20220.
27 Y. Yang, P. Gao, Y. Wang, L. Sha, X. Ren, J. Zhang, Y. Chen, T. Wu, P. Yang and X. Li, *Nano Energy*, 2017, **33**, 29–36.
28 Q. Huang, S. Tian, D. Zeng, X. Wang, W. Song, Y. Li, W. Xiao and C. Xie, *ACS Catal.*, 2013, **3**, 1477–1485.
29 G. Rajender, J. Kumar and P. K. Giri, *Appl. Catal., B*, 2018, **224**, 960–972.
30 O. Akhavan, R. Azimirad, S. Safa and M. M. Larijani, *J. Mater. Chem.*, 2010, **20**, 7386–7392.
31 Z. Hu, Y. Huang, S. Sun, W. Guan, Y. Yao, P. Tang and C. Li, *Carbon*, 2012, **50**, 994–1004.
32 L. Pan, S. Wang, J. Xie, L. Wang, X. Zhang and J.-J. Zou, *Nano Energy*, 2016, **28**, 296–303.
33 L. Pan, S. Wang, J.-J. Zou, Z.-F. Huang, L. Wang and X. Zhang, *Chem. Commun.*, 2014, **50**, 988–990.
34 S. D. Perera, R. G. Mariano, K. Vu, N. Nour, O. Seitz, Y. Chabal and K. J. Balkus, *ACS Catal.*, 2012, **2**, 949–956.
35 L. Y. Kunz, B. T. Diroll, C. J. Wrasman, A. R. Riscoe, A. Majumdar and M. Cargnello, *Energy Environ. Sci.*, 2019, **12**, 1657–1667.
36 T. Bak, M. K. Nowotny, L. R. Sheppard and J. Nowotny, *J. Phys. Chem. C*, 2008, **112**, 13248–13257.